RESEARCH ARTICLE

Key Points:
- We present detailed 3-D images of V_p and V_s for the upper mantle below the ME and NMSZ
- A prominent low-velocity anomaly with similar V_p and V_s anomalies is imaged in the upper mantle
- Regions of similar high V_p and V_s anomalies present above and to the sides of the low-velocity anomaly

A joint local and teleseismic tomography study of the Mississippi Embayment and New Madrid Seismic Zone

Cecilia A. Nyamwandha[1], Christine A. Powell[1], and Charles A. Langston[1]

[1]Center for Earthquake Research and Information, University of Memphis, Memphis, Tennessee, USA

Abstract Detailed, upper mantle *P* and *S* wave velocity (V_p and V_s) models are developed for the northern Mississippi Embayment (ME), a major physiographic feature in the Central United States (U.S.) and the location of the active New Madrid Seismic Zone (NMSZ). This study incorporates local earthquake and teleseismic data from the New Madrid Seismic Network, the Earthscope Transportable Array, and the FlexArray Northern Embayment Lithospheric Experiment stations. The V_p and V_s solutions contain anomalies with similar magnitudes and spatial distributions. High velocities are present in the lower crust beneath the NMSZ. A pronounced low-velocity anomaly of ~ −3%−−5% is imaged at depths of 100–250 km. High-velocity anomalies of ~ +3%–+4% are observed at depths of 80–160 km and are located along the sides and top of the low-velocity anomaly. The low-velocity anomaly is attributed to the presence of hot fluids upwelling from a flat slab segment stalled in the transition zone below the Central U.S.; the thinned and weakened ME lithosphere, still at slightly higher temperatures from the passage of the Bermuda hotspot in mid-Cretaceous, provides an optimal pathway for the ascent of the fluids. The observed high-velocity anomalies are attributed to the presence of mafic rocks emplaced beneath the ME during initial rifting in the early Paleozoic and to remnants of the depleted, lower portion of the lithosphere.

1. Introduction

The Mississippi Embayment (ME) is a large SSW plunging sedimentary basin in the South-Central United States filled with unconsolidated Upper Cretaceous and younger sediments [*Cox and Van Arsdale*, 2002]. Extensional features developed during the breakup of supercontinent Rodinia in Early Cambrian time lie below the ME [e.g., *Thomas*, 2006; *Hao et al.*, 2015]. The Reelfoot Rift is the most recognizable feature, but the entire embayment is underlain by rifted crust [*Johnson et al.*, 1994; *Cox and Van Arsdale*, 1997; *Cox et al.*, 2001]. Following *Thomas* [1991], we refer to the entire rift complex as the Mississippi Valley Graben (MVG). The active New Madrid Seismic Zone (NMSZ) is located within the Reelfoot Rift, near the northern terminus of the ME [*Van Arsdale et al.*, 2007] (Figure 1). Three significant ($M_w > 7$) NMSZ earthquakes occurred in the winter of 1811–1812 [*Nuttli*, 1973; *Johnston*, 1996; *Hough et al.*, 2000; *Van Arsdale and Cupples*, 2013], and paleoseismic evidence indicates a repeat time of about 500 years for events of similar magnitude [*Tuttle et al.*, 2002; *Van Arsdale et al.*, 2012]. The spatial correlation of the NMSZ and the ME is probably not coincidental and suggests that earthquake occurrence is linked to the tectonic processes that formed the embayment. The ME region has a complex tectonic history involving initial rifting, reactivation of rift faults in the Late Paleozoic (~290 Ma), passage of a hotspot in mid-Cretaceous time, and most recently, exposure to flat slab subduction.

Several models have been proposed for the ME subsidence and for the generation of earthquakes in the NMSZ. Most models for ME subsidence are associated with the opening of the Gulf of Mexico [*Wolaver et al.*, 2012] in Triassic/Jurassic time [*Ervin and McGinnis*, 1975; *Kane et al.*, 1981; *Braile et al.*, 1986], but *Cox and Van Arsdale* [1997] argue convincingly for a more recent development associated with passage of the Bermuda hotspot across the southern portion of the ME in mid-Cretaceous time. According to *Cox and Van Arsdale* [1997], ME subsidence began in the Late Cretaceous and ended by mid-Eocene.

Models that are specific to the NMSZ seismicity are numerous and include reactivation of favorably oriented rift faults in the present-day stress field [*Hildenbrand et al.*, 1977; *Sykes*, 1978; *Braile et al.*, 1986; *Cox and Van Arsdale*, 1997], increased differential stress from intrusions [*Kane*, 1977; *McKeown*, 1978], and deglaciation of the Laurentide ice sheet [*Grollimund and Zoback*, 2001]. Other proposed causes for the seismicity include a localized gravitational force produced by a dense, lower crustal intrusion [*Grana and Richardson*, 1996;
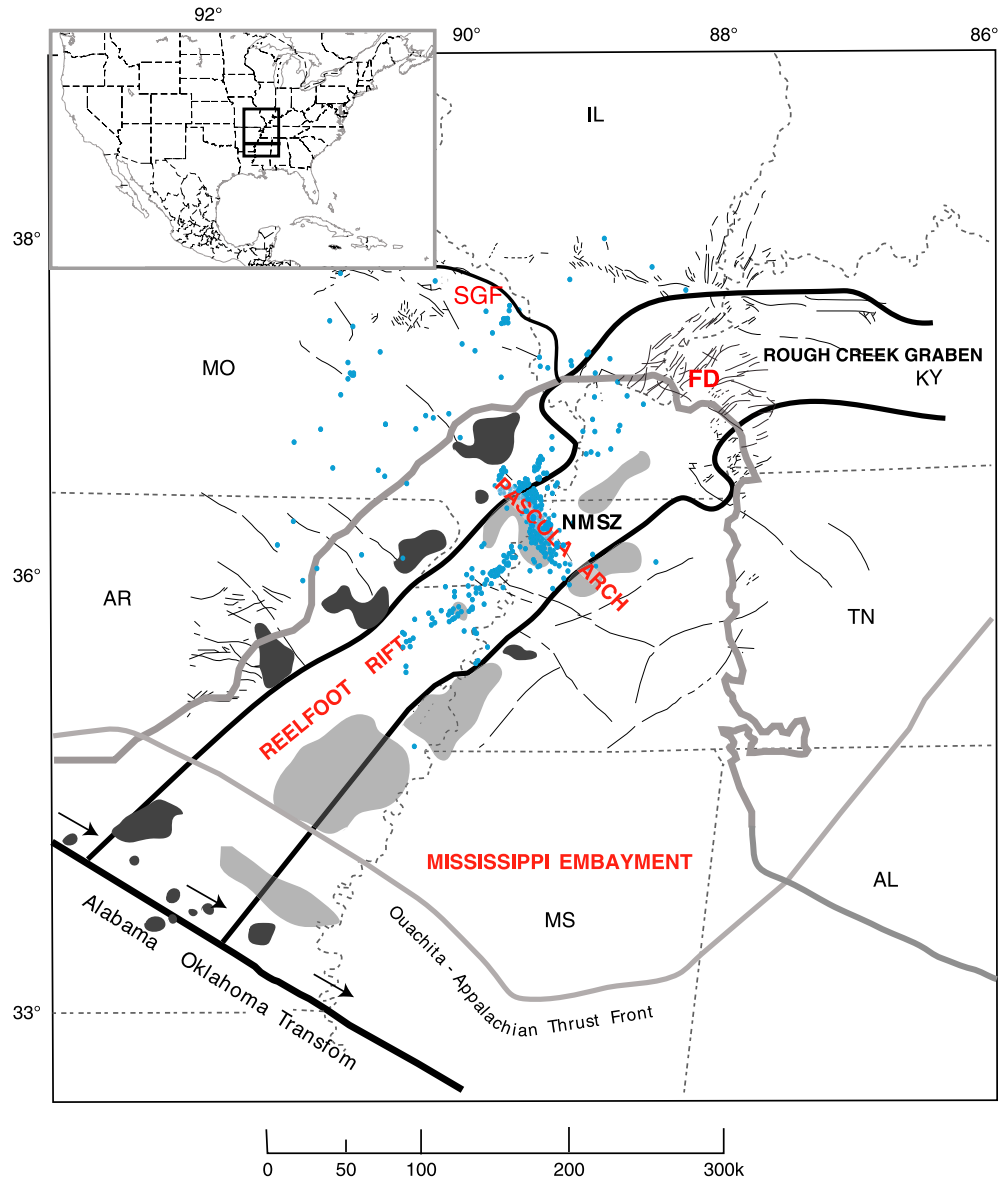
Figure 1. Major features of the study area. Inset gives location of the figure (large rectangle) and region covered by the inversion model (small rectangle). Thick gray line: outline of the Mississippi Embayment; thin black lines: Reelfoot Rift; thick black line: Alabama-Oklahoma transform fault; blue dots: earthquakes; black bodies: dense, mafic intrusions; light gray bodies: intrusive complexes. NMSZ: New Madrid Seismic Zone; FD: Fluorspar District; SGF: St. Genevieve Fault. Arrows indicate the possible hotspot track. Minor faults are shown as thin lines. AR, Arkansas; MO, Missouri; IL, Illinois; AL, Alabama; MS, Mississippi; KY, Kentucky; TN, Tennessee.

Pollitz et al., 2001; *Zhang et al.*, 2009a], the presence of a low-viscosity lower crust that transfers deviatoric stresses to the upper crust [*Kenner and Segall*, 2000], and stress related to the Farallon slab beneath the ME [*Forte et al.*, 2007]. There is neither an agreed upon cause for the NMSZ nor consensus regarding the hazard it presents to the region [e.g., *Boyd et al.*, 2015].

Recent tomography studies involving EarthScope USArray transportable (TA) stations indicate the presence of low velocities in the mantle below the ME. Low *S* wave velocity (V_s) values are determined from surface wave imaging [*Pollitz and Mooney*, 2014], and low *P* wave velocity (V_p) is found in a travel time inversion study using local and teleseismic earthquakes [*Chen et al.*, 2014]. Different reasons for the low velocities are offered in these studies. The main objective of our study is to develop better-resolved 3-D V_p and V_s models for the mantle below

the ME lithosphere using high-quality data from densely and uniformly distributed seismic networks. We use data recorded by TA stations, New Madrid broadband stations managed by the Center for Earthquake Research and Information (CERI), and stations associated with the Northern Embayment Lithospheric Experiment (NELE). NELE is an EarthScope Flexarray (FA) experiment designed to investigate velocity structure in the lithosphere. The availability of V_p and V_s models will place better constraints on the origin of the low mantle velocities and will provide insight into the conditions that are controlling earthquake generation in the NMSZ.

2. Previous Work

Several geophysical studies investigating crustal and upper mantle velocity structure have been carried out in the region surrounding the NMSZ. Interpretations of potential field data and active source reconnaissance seismic refraction and reflection experiments suggest significant crustal heterogeneity beneath the embayment related to a long and complex geological history of rifting, uplift, and subsidence [*Mooney et al.*, 1983; *Thomas*, 1985, 1991; *Catchings*, 1999]. Most notably, an anomalously fast (7.4 km/s) lower crust is found just above the Moho throughout most of the northern Mississippi Embayment [*McCamy and Meyer*, 1966; *Mooney et al.*, 1983; *Catchings*, 1999]. The time of emplacement of this feature termed the "mafic pillow" is enigmatic, as it could have been emplaced during initial rifting or during reactivation of rift faults in Permian or Cretaceous time.

A regional body wave and surface wave tomography study by *Bedle and Van der Lee* [2006] indicates that the upper mantle beneath the northern ME has relatively low *S* wave velocity. *Zhang et al.* [2009a] modeled the lithospheric velocity structure below the NMSZ by combining local *P* wave and teleseismic travel time data. Their results show that the lower crust and upper mantle beneath the NMSZ consist of a local, NE-SW trending low-velocity anomaly. *Pollitz and Mooney* [2014] obtain a pronounced low *S* wave seismic velocity extending to at least 200 km depth in a surface wave tomography study using TA stations. They hypothesize that this mantle volume is weaker than its surroundings and that the MVG consequently has relatively low elastic plate thickness, which would tend to concentrate tectonic stress within this zone [*Pollitz and Mooney*, 2014].

Chen et al. [2014] determine a 3-D crust and upper mantle V_p model up to 400 km depth beneath the NMSZ using data recorded by the TA. They also observe the low-velocity zone in the mantle and speculate that it may have a lower shear strength and act as a viscously weak zone embedded in the lithosphere which would in turn concentrate tectonic stress and transfer stress to seismogenic faults in the upper crust, leading to large intraplate earthquakes in the NMSZ [*Zhao*, 2015].

3. Data and Tomographic Method

Our data set for the inversion consists of arrival times from local earthquakes and relative travel time residuals obtained from teleseismic earthquakes recorded over a 4 year period from 2011 to 2015.

3.1. Local Earthquake Data

Arrival times for the local earthquakes used for the velocity inversions are recorded by the New Madrid seismic network managed by the Center for Earthquake Research and Information (CERI) at the University of Memphis. Arrival times were also determined for the TA stations and the first deployment of NELE stations shown in Figure 2. We used 519 local earthquakes with $M \geq 2.0$ (Figure 2). All events have at least five recordings yielding ~15,000 *P* and ~14,000 *S* arrival times. There is little to no seismicity to the southeast of the region.

3.2. Teleseismic Data

The second data set consists of 282 teleseismic events (30° and 90° from the study area) with $M \geq 5.5$ and at least eight recordings (Figure 3). Recording stations are shown in Figure 4 and include all of the NELE stations. The NELE project was divided into two phases. Phase one consisted of 6 month deployments which begun in September 2011 and was completed in October 2013. The second phase saw the deployment of 51 broadband seismometers along three profiles from July 2013 to June 2015. The average station spacing of the NELE stations was ~20 km (Figure 4). Teleseismic *P* and *S* wave arrivals are picked using the method of *Lou et al.* [2013]; the multi-channel cross-correlation algorithm [*VanDecar and Crosson*, 1990] cross-correlates each possible pair of seismograms and uses a least squares method [*Lou et al.*, 2013] to calculate an
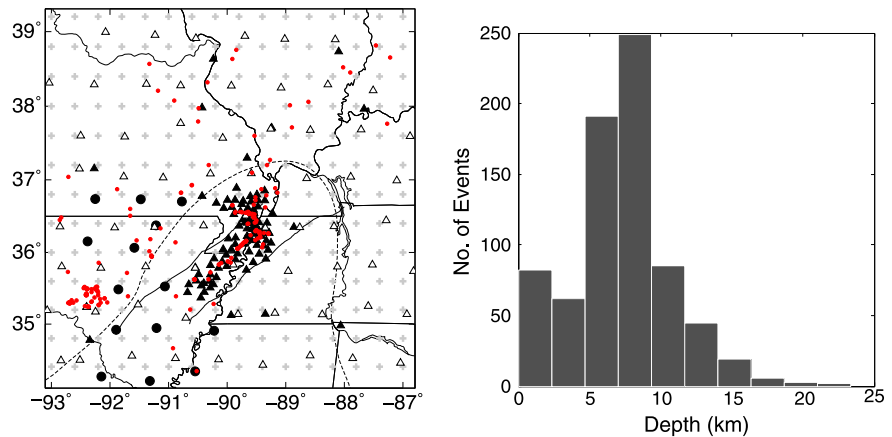
Figure 2. (left) Local earthquake (red circles) distribution and recording stations. USArray seismic stations (open triangles), 6 month NELE flex array deployments (black circles), New Madrid network stations (black triangles), and the inversion grid node locations (gray crosses). (right) Distribution of the events with depth.

optimized set of ~13,000 P and ~10,000 S relative arrival times. The measured arrival times are then used to calculate relative travel time residuals.
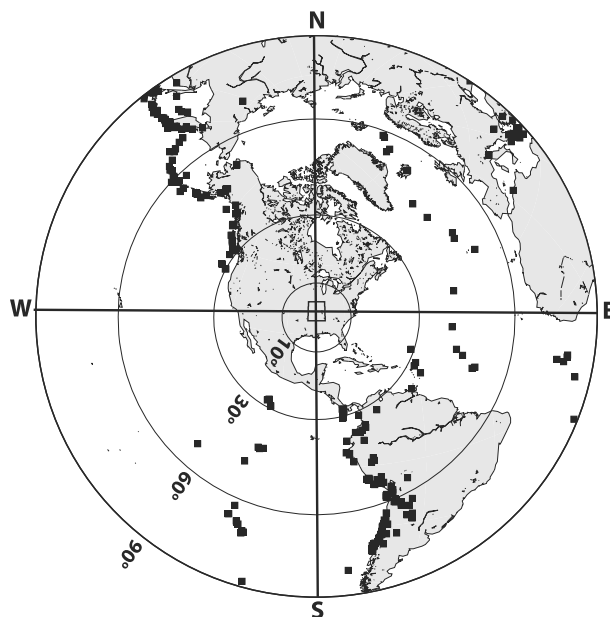
3.3. Inversion

We use the joint inversion method of *Zhao et al.* [1994] to obtain the 3-D V_p and V_s models of the crust and upper mantle. This technique is based on the *Paige and Saunders* [1982] Least Squares algorithm. A 3-D ray tracer is used for calculation of theoretical travel times and raypaths [*Zhao et al.*, 1992; *Zhao et al.*, 1996]. Optimal grid spacing is found by testing a range of node separations and determining the minimum root-mean-square travel time residual. The selected grid has 13 nodes in the latitudinal direction and 16 in the longitudinal direction with an interval of 0.40° (~40 km). For the vertical direction, 22 layers of varying intervals are set up in the crust and upper mantle. We simultaneously invert for hypocentral parameters of the local earthquakes and the velocity perturbations at the 4576 (13 × 16 × 22) grid nodes.

Figure 3. Epicentral locations of 282 teleseismic events (black squares) used in this study.

For the crust we use the 1-D starting model of *Pujol et al.* [1997] as outlined in *Powell et al.* [2010] (Table 1), and for the mantle, we use the International Association of Seismology and Physics 1991 model [*Kennett and Engdahl*, 1991] (Figure 5).
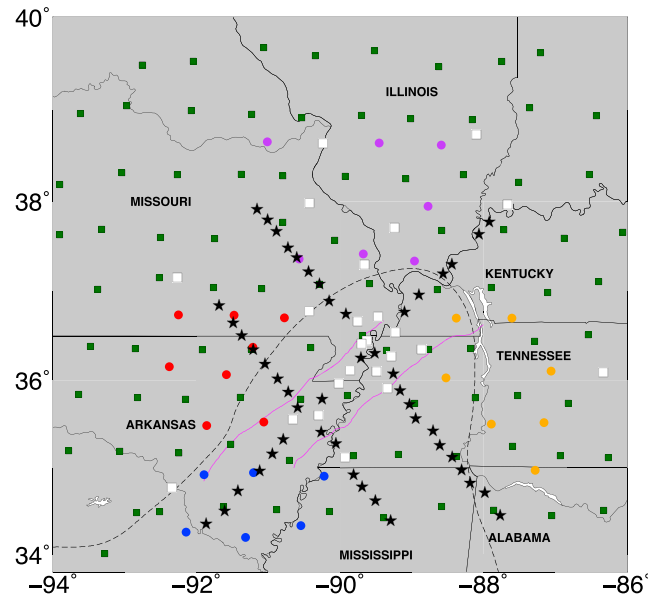
We use two kinds of regularization to add stability to the inversion and obtain a smooth model [*Zhao et al.*, 1992]. The optimal values of the damping and smoothing parameters obtained after several tomographic inversions are 10.0 and 20.0, respectively, for the P wave solution and 5.0 and 20.0, respectively, for the S wave solution. We use the method of *Zhao et al.* [1994] for the inversion taking into account only grid nodes with hit counts greater than 10.

3.4. Resolution

The spatial resolution of the estimated model can be affected by errors in the

Figure 4. NELE project stations. Green squares are the USArray seismic stations; blue, purple, orange, and red circles are the 6 month NELE FA deployments; white squares are the New Madrid broadband stations; and black stars are the NELE linear array stations.

data and ray coverage in the target study area. To test the resolution of our data set, we create a synthetic checkerboard model by assigning alternating two positive and two negative V_p and V_s perturbations of 6% to the 3-D grid nodes (Figure 6). Synthetic travel times are calculated for the checkerboard model using the same earthquake locations and stations as those in the real data set [*Huang and Zhao*, 2009]. The synthetic data are then inverted using the same starting velocity model, inversion algorithm, and inversion parameters used for the real data [*Zhao*, 2004]. The checkerboard is correctly reconstructed for most of the upper mantle, but resolution is low in the upper crust (Figures 7 and 8).

4. Results

Figures 9 and 10 show the V_p and V_s tomography solutions at six depths. The P and S wave velocity solutions are very similar regarding the spatial distribution of the anomalies and anomaly magnitudes. In agreement with previous studies, we observe high V_p and V_s velocities in the crust below 20 km depth and a pronounced low-velocity feature extending to ~250 km depth in the upper mantle. The NE-SW trending low-velocity feature is most evident at depths of 100–200 km where it is approximately 100 km wide and is similar in magnitude (~ −3% to −5%) in both the V_p and V_s solutions. This low-velocity zone is contained primarily in the mantle below the ME. For both V_p and V_s solutions, regions of high velocity (~ + 3% to +4%) are imaged along the sides and top of the low-velocity anomaly at depths of 80–160 km. Cross sections shown in Figure 11 reveal that the prominent low-velocity feature dips to the southwest.

Synthetic models are constructed for several prominent velocity features to investigate the reliability of the V_p and V_s solutions. The input model is shown in Figures 12a and 12b. Following the same inversion procedure as that of the checkerboard resolution tests, we observe that the recovered features are reproduced reliably. Some streaking is found to the northeast in V_s profile AA' and high-velocity artifacts with magnitudes less than 1% are present in profile BB'. The results show that the dip of the major velocity features to the southwest is not the result of streaking and the large-magnitude high-velocity features are not artifacts.

5. Discussion

Many intriguing features are observed in our P and S wave velocity models that could pertain to tectonic processes currently affecting the ME and the location of the NMSZ. Several velocity anomalies imaged in our study are present in previously determined V_p and V_s models for the Central U.S. These include the high velocities found in the lower crust [*Zhang et al.*, 2009b; *Pollitz and Mooney*, 2014] and a region of low velocity in the mantle [*Pollitz and Mooney*, 2014; *Chen et al.*, 2014; *Schmandt and Lin*, 2014]. *Pollitz and Mooney* [2014]

Table 1. One-Dimensional P and S Wave Velocity Models

Depth (km)	V_p (km/s)	V_s (km/s)	Description
0.00–0.65	1.8	0.72	Unconsolidated Upper Cretaceous to recent sediments
0.65–2.65	6.02	3.48	Late Cambrian–Early Ordovician Knox dolomite and limestone
2.65–4.65	4.83	2.79	Early–Middle Cambrian Elvis Shale
4.65–17.0	6.17	3.56	Precambrian crystalline upper crust
17.0–Moho	6.6	3.8	Precambrian crystalline lower crust
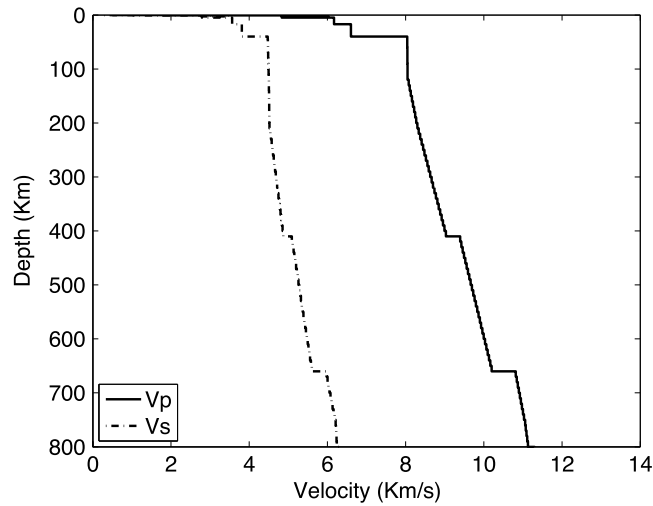
**Figure 5.** One-dimensional P and S wave starting velocity models.

attribute the low V_s anomalies to compositional changes produced by infiltration of melt by the Bermuda hotspot leading to metasomatism of existing mantle peridotite or emplacement of fertile mantle. *Chen et al.* [2014] attribute the low V_p anomalies to hot, wet upwelling flow from a portion of the Farallon slab stalled below the ME. Our study is the first to present both V_p and V_s models for the ME region and at unprecedented resolution within the mantle. Availability of both V_p and V_s models places restrictions on the origin of the observed mantle velocity anomalies and, as discussed below, supports the interpretation of *Chen et al.* [2014].

In most tomographic studies investigating upper mantle velocities, the V_p and V_s anomaly magnitudes are dissimilar [e.g., *Schmandt and Lin*, 2014]. This is because V_p and V_s are affected differently by the three main factors that contribute to the velocity anomalies: temperature variations, the presence of fluids, and changes in composition. In general, V_s is more sensitive to changes in these variables than V_p. In our study, any causative set of conditions will have to account for V_p and V_s anomalies with similar magnitudes and almost no variation in V_p/V_s. This set of circumstances is not without precedence; we note that V_p and V_s anomalies with the same magnitudes are found in the mantle below the North China Craton [*Santosh et al.*, 2010].

Various authors have studied the sensitivity of V_p and V_s to composition and temperature [*Lee*, 2003; *Schutt and Lesher*, 2006; *Wagner et al.*, 2008]. *Lee* [2003] investigate the effects of mantle compositional variations on density and seismic velocities for a suite of upper mantle peridotites spanning the primary compositional range of fertile (magnesium number (Mg#) $= 100 \times$ Mg/(Mg + Fe) of 86–88) to highly residual compositions (Mg# of 93–94) [*Lee*, 2003]. According to this study, increased magnesium number would lead to a significant increase in shear wave velocity, whereas V_p is insensitive to Mg#. *Lee* [2003] determines the relationship $V_s = 0.0143$ Mg# $+ 3.53$ from a linear regression of V_s on Mg#. V_s can be expected to vary by ~2.5% between Mg# 86 and Mg# 94. We observe a decrease of ~6% in V_s in the upper mantle. Using the regression parameters, a Mg# of 74 is needed to produce a 6% decrease in V_s from a representative starting value of 4.88 km/s. This Mg# falls well outside of the range for upper mantle peridotites. In addition, *Lee* [2003] shows that the V_p/V_s ratio is much more sensitive to compositional changes than changes in temperature. According to *Lee* [2003], the relative effect of temperature and Mg# change on V_p/V_s is roughly ΔMg# ~ -0.1 ΔT. A refertilized/primitive mantle with lower Mg# would produce a significant low V_s anomaly, little to no V_p anomaly, and an increased V_p/V_s ratio. We observe low V_s and V_p anomalies of comparable magnitude below the ME and minimal variations in V_p/V_s. Thus, compositional variations involving the presence of refertilized or primitive mantle alone would not be expected to produce the observed anomalies.

Temperature effects will dominate mantle lateral velocity variations in the absence of strong compositional variations [e.g., *Karato*, 1993; *Cammarano et al.*, 2003]. The study by *Cammarano et al.* [2003] investigates the relationship between upper mantle thermal structure and seismic velocity anomalies. They demonstrate that the sensitivity
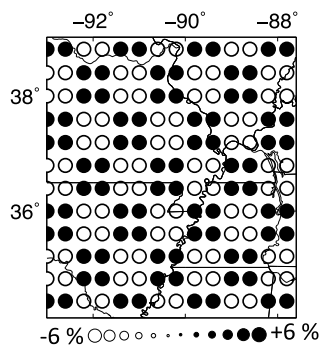
Figure 6. Input checkerboard model for inversion results shown in Figures 7 and 8.
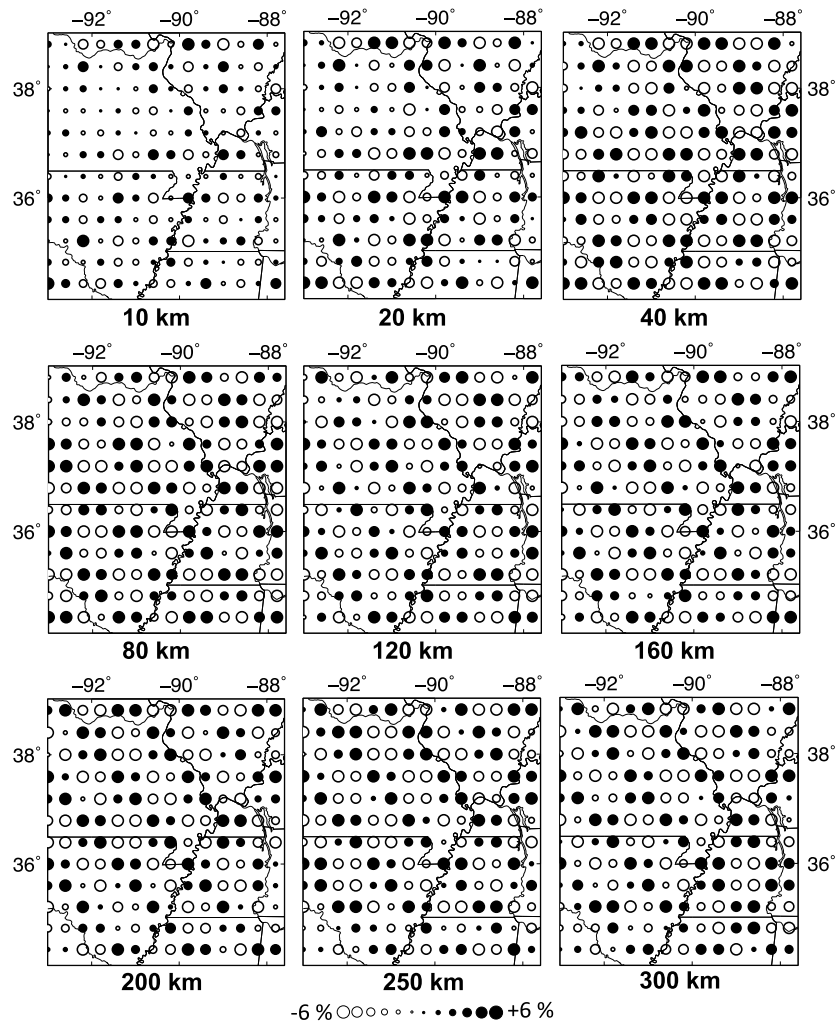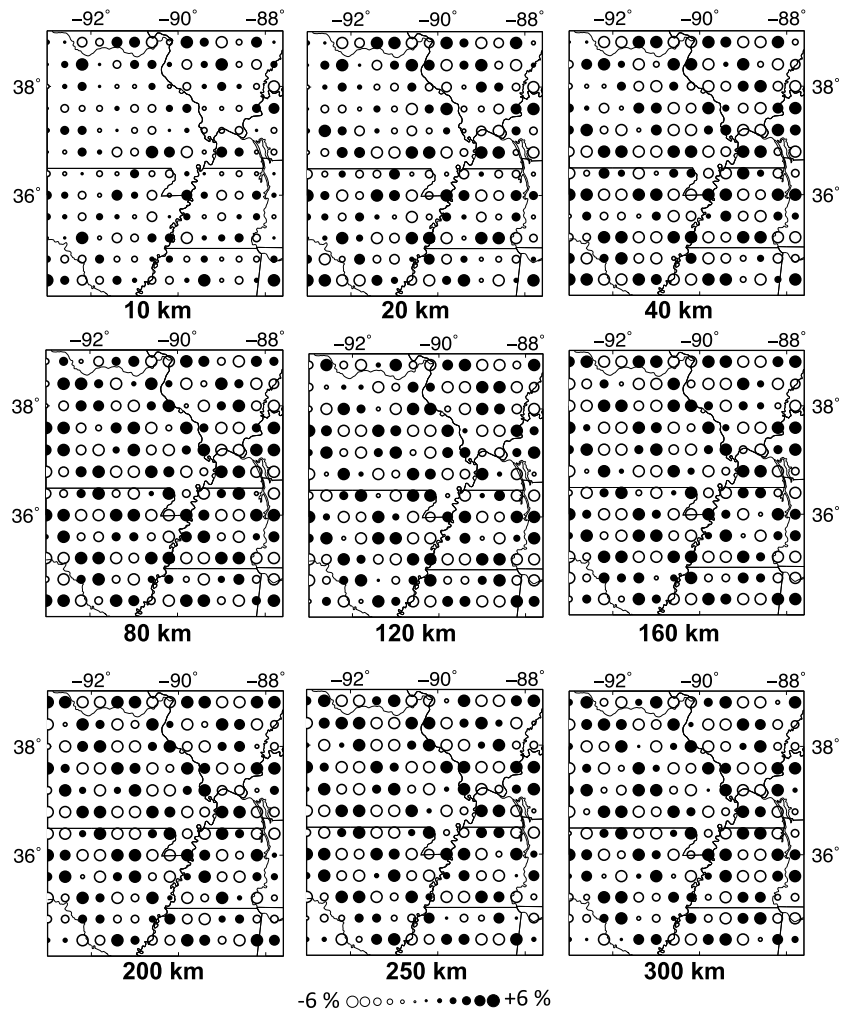
Figure 7. Recovered V_p checkerboard model from input model shown in Figure 6.

of velocity to temperature along a 1300°C adiabat decreases with increasing depth. For V_p, the change is from $-0.75 \pm 0.15\%$ per 100°C at 200 km to $-0.23 \pm 0.05\%$ per 100°C at 800 km. For V_s, the change is from $-1.30 \pm 0.30\%$ per 100°C at 200 km to $-0.45 \pm 0.10\%$ per 100°C at 800 km depth. For our study involving velocity anomalies at or above 250 km, these results would suggest that within the error bounds stated above, it would require an excess temperature of ~400 ± 100°C to produce the observed low V_s anomalies and ~670 ± 140°C to produce the low V_p anomalies. An increase in temperature of this amount would produce melting and very large, negative V_s anomalies [*Hammond and Humphreys*, 2000]. Thus, the observed anomalies cannot be attributed to elevated temperatures alone.

Some increase in temperature may be present in the mantle below the ME due to the mid-Cretaceous passage of the Bermuda hotspot and provide justification below. Passage of the hotspot probably elevated temperatures sufficiently to produce melting in parts of the lithosphere below the ME, as evidenced by the presence of intrusions interpreted to be Cretaceous age in and adjacent to the Reelfoot Rift [e.g., *Hildenbrand and Hendricks*, 1995; *Cox and Van Arsdale*, 2002; *Hao et al.*, 2015] (Figure 1). However, *Pollitz and Mooney* [2014] argue for a lack of significant residual thermal anomaly from the hotspot. This is supported by the subsidence history of the ME, which was complete by Late Eocene [*Cox and Van Arsdale*, 2002].

Eaton and Frederiksen [2007] conduct a numerical experiment to check evolution of a thermal anomaly 120 Ma following passage over the Great Meteor hotspot and determined that the residual thermal anomaly would be about 80°C and concentrated at 200 km. The thermal models of *Chu et al.* [2013] indicate that a

Figure 8. Recovered V_s checkerboard model from input model shown in Figure 6. Checkerboard recovery is comparable to the recovery found for the P wave velocity solution.
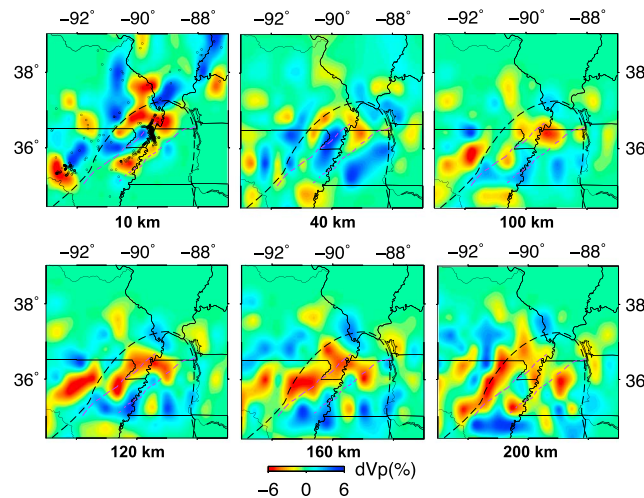
Figure 9. V_p tomography solution at six depths. Negative and positive velocity perturbations are indicated by red and blue colors, respectively. Black and purple dashed lines delimit the ME and Reelfoot Rift, respectively. Black circles are the local earthquakes.

residual temperature increase from a postulated mantle hotspot 74 Ma after impacting the Central U.S. lithosphere could produce V_p anomalies of roughly 2%. This value is much lower than our observed anomalies. This suggests that residual, elevated temperature due to the Cretaceous passage of the Bermuda hotspot cannot be the only reason for the observed low-velocity anomalies but may be a contributing factor.

The presence of water in the mantle can reduce both V_p and V_s [*Karato*, 2003; *Jacobsen et al.*, 2004; *Bastow et al.*, 2008; *Eaton et al.*, 2009; *Mao et al.*, 2011] and could explain low-velocity anomalies in the upper mantle [*Van der Lee et al.*, 2008; *Santosh et al.*, 2010; *Tian and Zhao*, 2011; *Pollitz and Mooney*, 2014;
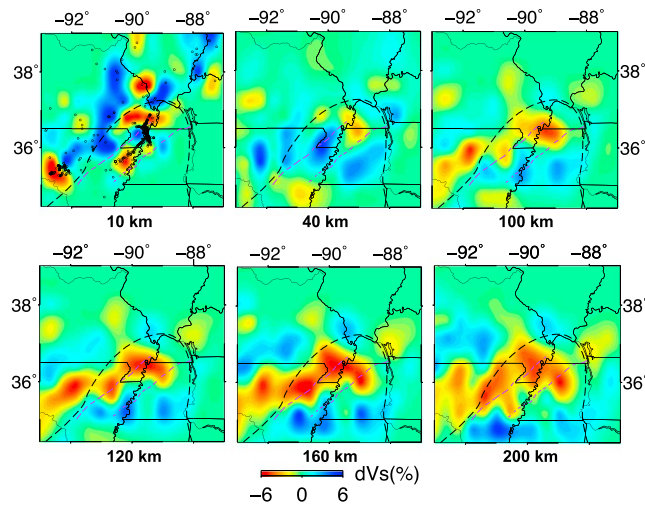
Figure 10. V_s tomography solution at six depths. Description is the same as in Figure 9.

Chen et al., 2014]. Water can reduce mantle seismic velocities by increasing the water content in minerals such as olivine, resulting in increased anelasticity and attenuation [*Dixon et al.,* 2004]. Water can also reduce V_P and V_s by metasomatic alteration of mantle peridotite (or eclogite) [*Sobolev and Babeyko,* 1994; *Goes and Van der Lee,* 2002; *Mainprice et al.,* 2008; *Pollitz and Mooney,* 2014], resulting in the formation of low-velocity minerals such as phlogopite, chlorite, and talc [*Sommer and Gauert,* 2011]. Possible sources of elevated water levels include rising, hydrated asthenosphere at hotspot locations [*Pollitz and Mooney,* 2014] and dehydration of descending slabs [*Dixon et al.,* 2004; *Santosh et al.,* 2010; *Chen et al.,* 2014].
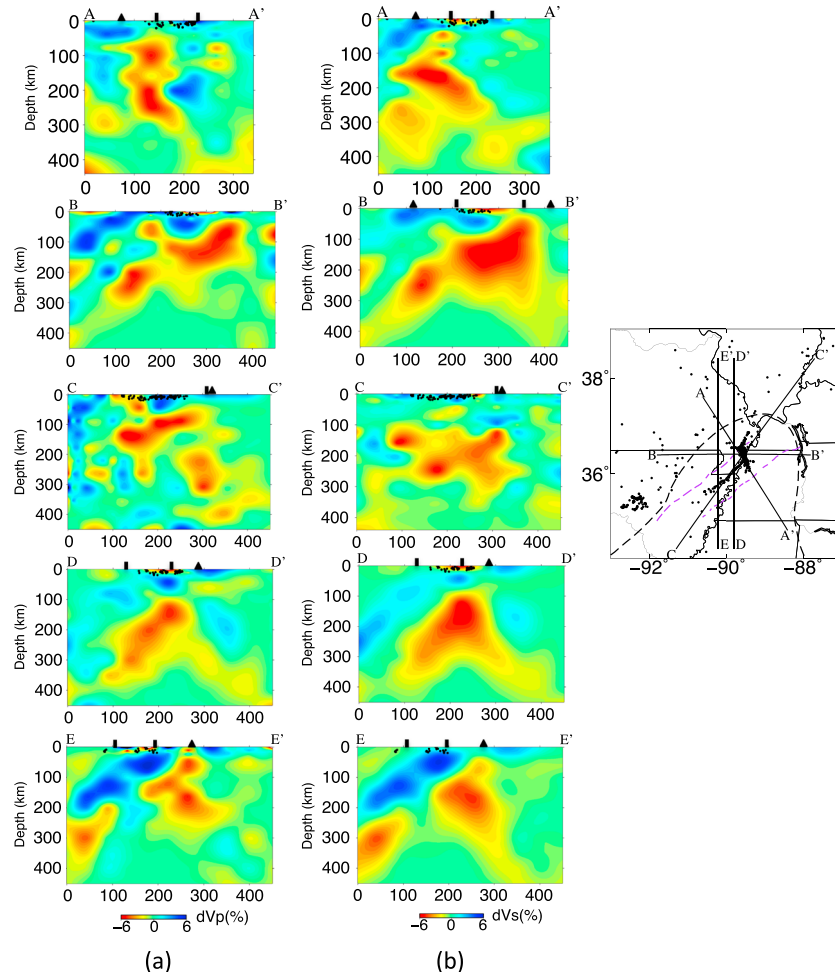
Figure 11. Vertical cross sections of the (a) V_p and (b) V_s tomography results. Black circles are the local earthquake locations. Black triangles delimit the ME, and the black bars delimit the Reelfoot Rift. Profile locations are shown to the right.
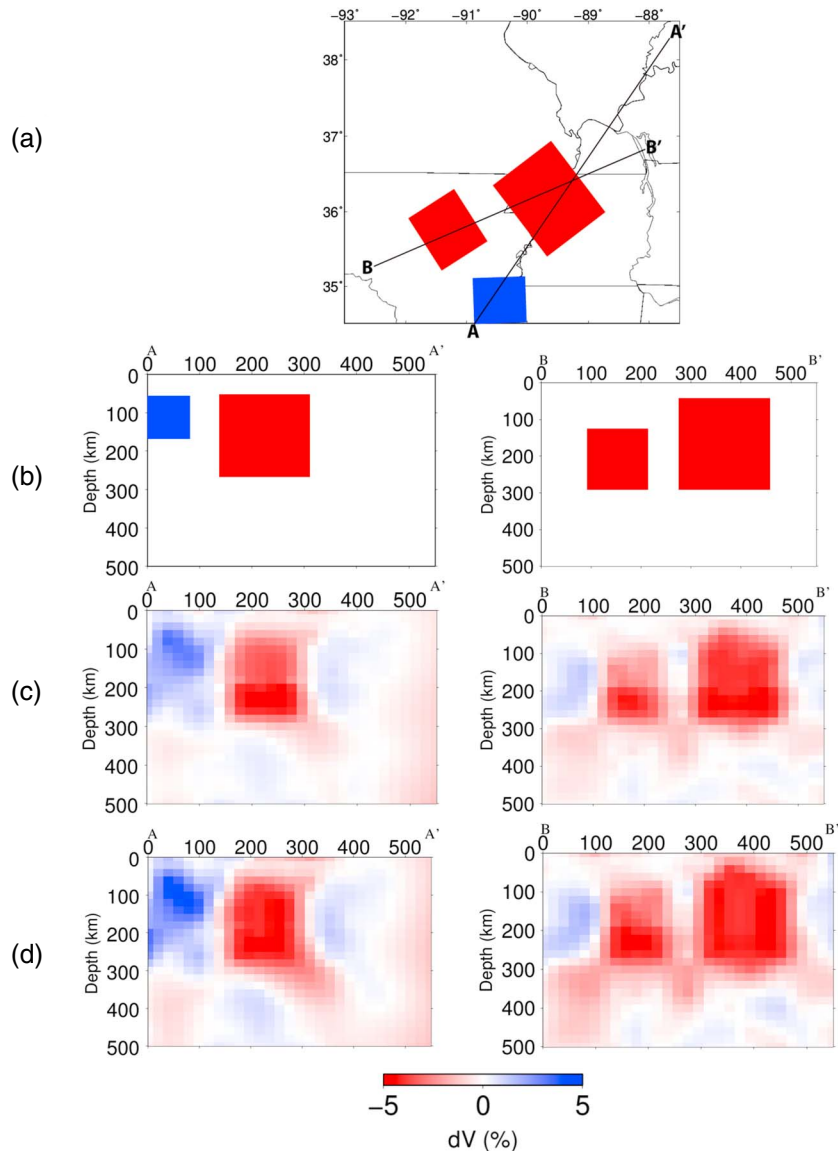
Figure 12. (a) Map view of input synthetic model −5% (red) and +5% (blue) velocity anomalies relative to the 1-D starting model. (b) Cross sections through the input model. (c) V_p inversion results and (d) V_s inversion results.

The presence of hydrated mantle probably plays a significant role in the creation of our observed low-velocity anomalies below the ME.

Quantifying the effect of fluids on upper mantle velocities is challenging. *Schutt and Lesher* [2010] perform a component analysis on garnet peridotite xenoliths from the Kaapvaal Craton to quantify factors controlling seismic velocity variations within metasomatically altered cratonic mantle. They find that orthopyroxene enrichment, possibly due to silica addition by subduction zone fluids, reduces V_p by about 1.2% but has little effect on V_s. *Christensen* [1966] and *Miller and Christensen* [1997] derive a relationship between wt % H_2O and V_p for common ultrabasic upper mantle rocks:

H_2O (wt%) = (32 ± 1) − (3.79 ± 0.18) V_p (km/s). Starting with a representative velocity of 8.44 km/s, addition of 1.96 wt % H_2O is required to produce the maximum observed (−6%) low V_p anomalies. This amount of H_2O enrichment is not uncommon, particularly in the presence of partially serpentinized ultramafic rocks [*Carlson and Miller*, 2003]. Quantitative studies exist for two common minerals in the mantle transition zone. *Jacobsen et al.* [2004] determine that V_p and V_s are reduced by about 40 m/s for every 1000 ppm weight (0.1 wt %) H_2O added to iron-bearing ringwoodite. Bulk V_p and V_s for hydrous iron-bearing ringwoodite are about 4.4 and
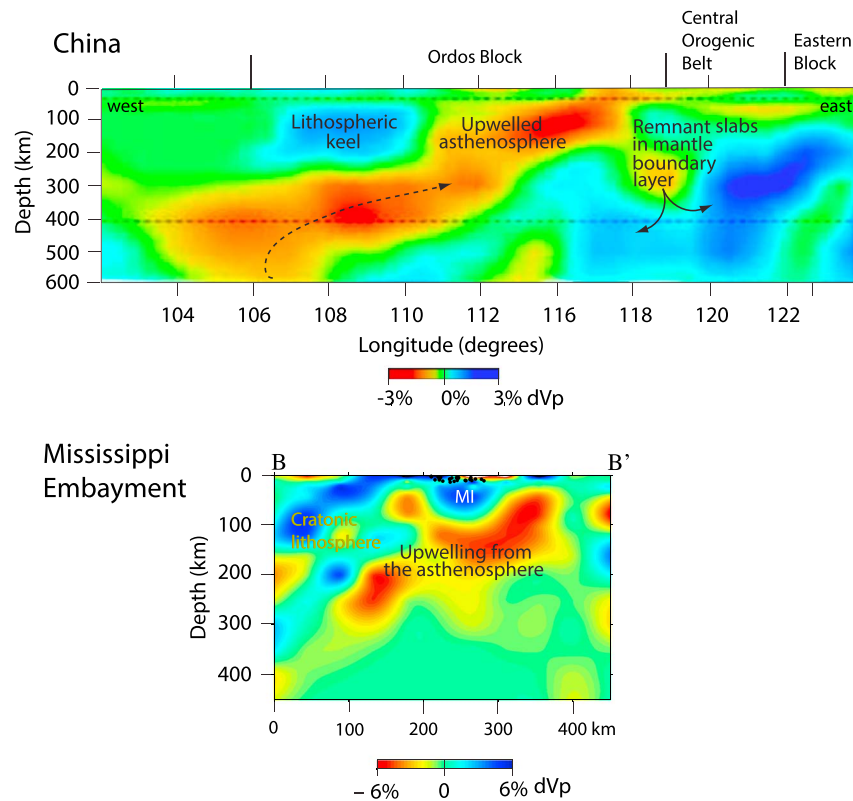
Figure 13. (top) Vertical cross section of V_p anomalies across the North China Craton at 40°N displaying the low-velocity zone extending from the stalled Pacific slab to the near surface. Upper dashed line is the Moho and lower dashed line is the 410 km discontinuity. Adapted from *Santosh et al.* [2010], indicating their interpretation of the velocity anomalies. (bottom) Cross-section BB′ from Figure 11 with our interpretation of the velocity anomalies below the ME. MI is the mafic intrusion.

6.5% slower, respectively, than for dry iron-bearing ringwoodite. *Mao et al.* [2011] determine that V_p and V_s of hydrous iron-bearing wadsleyite are about 2% slower than dry iron-bearing wadsleyite at transition zone pressures.

We provide a possible interpretation for the observed high- and low-velocity anomalies below the ME that is tied to the major tectonic events that affected the region.

Stage 1   Precambrian: The ME is underlain by ~1.45–1.35 Ga lithosphere that is part of the proto-Laurentia Craton [*Whitmeyer and Karlstrom*, 2007]. As is the case with stable Precambrian cratons, the litho-sphere would be expected to have a well-developed root (keel) consisting of dry, depleted mantle rocks [e.g., *Boyd*, 1989].

Stage 2   Latest Precambrian to Early Cambrian Mississippi Embayment rift complex: Disassembly of the supercontinent Rodinia produced the Iapetus Ocean and several rift-parallel, extensional features inboard from the rifted margin [*Thomas*, 1991, 2006]. The Reelfoot Rift (Figure 1) is the most recognizable feature, but the entire embayment is underlain by rifted crust [*Johnson et al.*, 1994; *Cox and Van Arsdale*, 1997; *Van Arsdale and Cox*, 2007]. Fault separation of the top of the basement rocks in the MVG is as much as 1.8 km [*Thomas*, 1991], indicating that rifting was not extensive. Modest extension of the basement is also indicated by deep reflection profiles [*Nelson and Zhang*, 1991]. There are no dated intrusions that can be associated with the rifting [*Hildenbrand and Hendricks*, 1995], but rifting may have resulted in magmatic underplating of the lower crust [*Braile et al.*, 1986; *Nelson and Zhang*, 1991; *Catchings*, 1999; *Pratt et al.*, 2013]. Rifting probably thinned the lithosphere to some extent and caused refertilization as depleted mantle lithosphere was replaced by asthenosphere. Fluids may also have been introduced, estab-lishing a weak zone that would be more easily reactivated and penetrated by future tectonic and

thermal events [*Cox and Van Arsdale*, 1997; *Ziegler and Cloetingh*, 2004; *Burov et al.*, 2007; *Villemaire et al.*, 2012].

Stage 3   Appalachian-Ouachita orogeny (refer to Figure 1 for named features): Closing of the Iapetus and Rheic Oceans during the formation of supercontinent Pangea reactivated MVG structures and produced compressional features including an elongate anticline paralleling the boundary faults of the Reelfoot Rift [*Thomas*, 1991]. Intrusions most likely of Permian age are present in the axis of the MVG (the Pascola Arch [*Hildenbrand*, 1985]), along structural features located just to the north of the MVG (e.g., the St. Genevieve Fault in southern Missouri and within the Illinois-Kentucky Fluorspar District [*Zartman*, 1977; *Hildenbrand*, 1985]), and in central Arkansas [*Zartman and Howard*, 1987]. The intrusions include kimberlite and lamprophyric dikes, suggesting mantle source rocks [e.g., *Xu*, 2001; *Griffin et al.*, 2011].

Stage 4   Cretaceous hotspot: A major thermal event affected the ME during mid-Cretaceous time (~100 Ma) resulting in the intrusion of a suite of ultramafic and alkali rocks [*Cox and Van Arsdale*, 1997; *Griffin et al.*, 2011] (Figure 1). Most sampled intrusions occur within the southern portion of the ME and display an age progression from northwest (oldest) to southeast (youngest). Syenites have also been drilled along the northern Reelfoot Rift axis, and the presence of multiple ultramafic and alkalic igneous intrusions along the axis and bounding faults of the northern Reelfoot Rift are inferred by potential field anomalies [*Hildenbrand et al.*, 1982; *Hildenbrand and Hendricks*, 1995]. The suite of intrusions suggests widespread, thermal modification of the mantle below what is now the ME [*Cox and Van Arsdale*, 2002]. *Cox and Van Arsdale* [1997] suggest that the intrusions were produced by passage of the Bermuda hotspot below the southern portion of the ME and support this with geologic evidence for the presence of an anticline with greater than 1 km of relief trending parallel to the axis of the ME. The uplift is attributed to thermal doming produced by emplacement of igneous material during passage of the hotspot, and the Bermuda hotspot track determined by *Duncan* [1984] crosses the southern ME in mid-Cretaceous time (Figure 1). The unusual suite of mid-Cretaceous igneous rocks including peridotite, lamprophyre, kimberlite, syenite, trachyte, phonolite, and carbonatite is compatible with a mantle hotspot source [*Cox and Van Arsdale*, 1997] as well as partial melting of continental crust [*Morris*, 1987].

The Bermuda hotspot track trends northwest-southeast, raising a question as to why passage of the hotspot would produce thermal doming and intrusions along the northeast trending ME. Geodynamic modeling indicates that the thickness and geometry of the continental lithosphere have a significant influence on the flow of hotspot material [*Villemaire et al.*, 2012]; in general, thick, stable cratonic keels deflect the flow of hotspot material toward regions of thinner lithosphere [*Sleep*, 1997; *Burov et al.*, 2007]. More significant ponding of hotspot material occurs in the regions of thinner lithosphere, and focusing of flow may enhance melting and magmatism [*Ebinger and Sleep*, 1998; *Sleep*, 2002; *Ziegler and Cloetingh*, 2004]. For example, *Villemaire et al.* [2012] attribute the presence of a pronounced low V_p anomaly in the mantle below a failed rift (the Ottawa-Bonnechere Graben) to focusing and emplacement of fertile melts during passage of the Great Meteor hotspot. Interaction of hotspots with rifted continental lithosphere can produce additional thinning, chemical alteration by metasomatism, and delamination [*Burov et al.*, 2007; *O'Reilly and Griffin*, 2010].In our case, the Bermuda hotspot track determined by *Duncan* [1984] coincides approximately with the trend of the Alabama-Oklahoma transform marking the edge of the craton [e.g., *Thomas*, 1991, 2006; *Cox et al.*, 2013] (Figure 1). The Alabama-Oklahoma transform was established during the breakup of Rodinia (stage 2 above) and forms the southern boundary of the Reelfoot Rift and other rifts below the ME. Thus, the thinned and mechanically weak lithosphere beneath the ME may have provided a favorable pathway for hotspot magma [*Cox and Van Arsdale*, 1997], resulting in additional thinning of the existing lithosphere and chemical alteration by partial melting and infiltration of fluids.

Stage 5   Influence of subducted slabs. The presence of subducted slabs may be influencing mantle flow and hydration in the eastern and Central U.S. [*Forte et al.*, 2007; *Van der Lee et al.*, 2008]. The existence of a high-velocity slab segment below 800 km is documented in several tomography studies and is interpreted as a portion of the Farallon slab [*Grand*, 2002; *Van der Lee and Frederiksen*, 2005; *Schmandt and Lin*, 2014]. In addition, high-resolution, finite-frequency body wave tomography studies indicate the presence of a large, flat slab segment stalled in the mantle transition zone below the Central U.S.

[*Sigloch et al.*, 2008; *Sigloch*, 2011; *Sigloch and Mihalynuk*, 2013]. The flat slab, called the Laramide slab by *Sigloch* [2011], exists in the depth range from 300 to roughly 700 km and has been present below the ME since approximately Paleocene time (65–70 Ma). We suggest that the presence of the stalled slab has a profound influence on the mantle below the ME and is a primary contributor to the observed velocity anomalies.

A stalled slab is also present in the transition zone below the eastern North China Craton, and distinct regions of high and low V_p and V_s anomalies are present in the upper mantle that are similar in appearance to those observed below the ME [*Santosh et al.*, 2010; *Tian and Zhao*, 2011]. As is the case for the ME, the V_p and V_s anomalies have the same magnitudes. Figure 13 illustrates V_p anomalies in an east-west cross section through the North China Craton at 40°N. A sharply defined low-velocity region extends from roughly 400 km to the near surface along a path that dips to the west and is bounded over part of its length by regions with high V_p and V_s anomalies. The low-velocity region is interpreted as hot, fluid-rich asthenosphere ascending from the mantle wedge above the stagnant Pacific slab [e.g., *Zhao*, 2015]. High-velocity regions are interpreted as remnants of the lithospheric keel above the low-velocity region and as remnant slabs below [*Santosh et al.*, 2010]. The ascending asthenosphere is associated with the Central Orogenic Belt, a thin zone in the lithosphere that experienced delamination following Early Mesozoic subduction and collision [*Tian and Zhao*, 2011]. This orogenic belt now acts a main conduit for hot, wet upwelling asthenosphere from the stagnant slab resulting in continued destruction of the lithosphere by thermal erosion and chemical metasomatism [*Santosh et al.*, 2010; *Tian and Zhao*, 2011].

The striking similarity between the velocity structure below the North China Craton and the ME suggests that similar mantle processes are affecting both regions. A stalled slab exists below both regions, and a well-defined, low-velocity anomaly extends from the asthenosphere to shallow depths in a location that experienced thinning due to prior tectonic activity. Similar to the situation for the North China Craton, we suggest that hot, hydrous, upwelling fluids from the stalled Laramide slab produce the low V_p and V_s anomalies below the ME. The thinned, weakened lithosphere below the ME provides the optimal pathway for the ascending fluids. *Chen et al.* [2014] offer a similar interpretation based upon V_p anomalies alone. We interpret the prominent high-velocity regions located above and to the sides of the low-velocity region as remnants of the depleted, lowermost lithosphere.

As is evident in Figure 13, the area affected by upwelling from the stagnant Pacific slab is much larger than the ME. The North China Craton has undergone a long and complicated decratonization process beginning in Late Paleozoic or Early Mesozoic time, and the flat Pacific slab has been present since the Early Mesozoic [*Li and Li*, 2007; *Zhu and Zheng*, 2009]. Consequently, the velocity anomalies in China developed over a much longer time period than the anomalies below the ME, and the low-velocity conduit for ascending asthenosphere is better established. Cenozoic age basalts in northern China are spatially correlated with the low-velocity zone in the mantle, and geochemistry links the basalts to the presence of a stagnant slab [*Kuritani et al.*, 2011; *Xu et al.*, 2012]. The situation in China suggests that continued upwelling of hot, hydrous fluids below the ME will result in further modification of the lithosphere, possibly leading to intrusive activity in the crust.

In all likelihood, the NMSZ is linked to the presence of the low-velocity region in the mantle below the ME. In our models, the low-velocity region underlies the Reelfoot Rift north of roughly 35.5°N (Figures 9–11). Most NMSZ earthquakes are located within the Reelfoot Rift, above the high-velocity region imaged in the lower crust (Figure 11). An exception is the portion of the Axial Fault south of roughly 36°N where earthquakes are scattered and terminate south of 35.5°N (profile CC′, Figure 11). The low-velocity region extends to very shallow depths below the high-velocity lower crust. The association of seismicity and velocity structure suggests that the low-velocity region may be acting as a zone of weakness, transferring stress to the stronger, overlying crust. The concept is similar to the model developed by *Kenner and Segall* [2000] for the NMSZ, but here the weak zone is located in the uppermost mantle, rather than in the lower crust. This variation on the model developed by *Kenner and Segall* [2000] may make more sense for the NMSZ, given the presence of the high-velocity, and presumably strong, lower crust and can be tested by numerical modeling.

6. Conclusions

We have determined detailed 3-D images of V_p and V_s for the upper mantle below the Mississippi Embayment. A prominent low-velocity anomaly defined by V_p and V_s anomalies of similar magnitude is imaged in the upper mantle. The low-velocity region dips to the southwest and extends to a depth of at least

300 km. Low velocities extend to shallow depths (about 50 km) below the northern end of the Reelfoot Rift. A region of high velocity in the lower crust separates the low velocities from the seismogenic upper crust hosting the NMSZ. Regions of high velocity with comparable V_p and V_s anomalies are present above and to the sides of the low-velocity region. In agreement with previous studies, we suggest that the lithosphere below the Mississippi Embayment was thinned and weakened by a long history of tectonic events including initial rifting and the passage of the Bermuda hotspot in the mid-Cretaceous. The warm, thin, and weak lithosphere provides a favorable pathway for hot fluids ascending from the flat Laramide slab that is stalled in the mantle transition zone below the embayment. The pronounced low-velocity region below the ME is attributed to the presence of residual heat associated with the Bermuda hotspot combined with the hot hydrated conditions established by the presence of the stalled slab. High-velocity regions in the lower crust are interpreted as mafic rocks emplaced beneath the ME during initial rifting in the Early Paleozoic, whereas high velocities in the mantle are interpreted as remnants of the depleted cratonic mantle lithosphere.

References

Bastow, I. D., A. A. Nyblade, G. W. Stuart, T. O. Rooney, and M. H. Benoit (2008), Upper mantle seismic structure beneath the Ethiopian hot spot: Rifting at the edge of the African low-velocity anomaly, *Geochem. Geophys. Geosyst.*, *9*, Q12022, doi:10.1029/2008GC002107.

Bedle, H., and S. Van der Lee (2006), Fossil flat-slab subduction beneath the Illinois basin, USA, *Tectonophysics*, *424*(1), 53–68.

Boyd, F. R. (1989), Compositional distinction between oceanic and cratonic lithosphere, *Earth Planet. Sci. Lett.*, *96*, 15–26.

Boyd, O. S., R. Smalley Jr., and Y. Zeng (2015), Crustal deformation in the New Madrid Seismic Zone and the role of postseismic processes, *J. Geophys. Res. Solid Earth*, *120*, 5782–5803, doi:10.1002/2015JB012049.

Braile, L. W., W. J. Hinze, G. R. Keller, E. G. Lidiak, and J. L. Sexton (1986), Tectonic development of the New Madrid rift complex, Mississippi Embayment, North America, *Tectonophysics*, *131*(1), 1–21.

Burov, E., L. Guillou-Frottier, E. D'Acremont, L. Le Pourhiet, and S. Cloething (2007), The plume head-lithosphere interactions near intra-continental plate boundaries, *Tectonophysics*, *434*(1-4), 15–38, doi:10.1016/j.tecto.2007.01.002.

Cammarano, F., S. Goes, P. Vacher, and D. Giardini (2003), Inferring upper-mantle temperatures from seismic velocities, *Phys. Earth Planet. Inter.*, *138*(3), 197–222.

Carlson, R. L., and D. J. Miller (2003), Mantle wedge water contents estimated from seismic velocities in partially serpentinized peridotites, *Geophys. Res. Lett.*, *30*(5), 1250, doi:10.1029/2002GL016600.

Catchings, R. D. (1999), Regional V_p, V_s, V_p/V_s and Poisson's ratios across earthquake source zones from Memphis, TN, to St. Louis, MO, *Bull. Seismol. Soc. Am.*, *89*, 1591–1605.

Chen, C., D. Zhao, and S. Wu (2014), Crust and upper mantle structure of the New Madrid Seismic Zone: Insight into intraplate earthquakes, *Phys. Earth Planet. Inter.*, *230*, 1–14.

Christensen, N. I. (1966), Elasticity of ultrabasic rocks, *J. Geophys. Res.*, *71*, 5921–5931, doi:10.1029/JZ071i024p05921.

Chu, R., W. Leng, D. V. Helmberger, and M. Gurnis (2013), Hidden hotspot track beneath the eastern United States, *Nat. Geosci.*, *6*(11), 963–966.

Cox, R. T., and R. B. Van Arsdale (1997), Hotspot origin of the Mississippi Embayment and its possible impact on contemporary seismicity, *Eng. Geol.*, *46*(3), 201–216.

Cox, R. T., and R. B. Van Arsdale (2002), The Mississippi Embayment, North America: A first order continental structure generated by the Cretaceous superplume mantle event, *J. Geodyn.*, *34*(2), 163–176.

Cox, R. T., R. B. Van Arsdale, and J. B. Harris (2001), Identification of possible Quaternary deformation in the northeastern Mississippi Embayment using quantitative geomorphic analysis of drainage-basin asymmetry, *Geol. Soc. Am. Bull.*, *113*(5), 615–624.

Cox, R. T., J. Harris, S. Forman, T. Brezina, J. Gordon, C. Gardner, and S. Machin (2013), Holocene faulting on the Saline River fault zone, Arkansas, along the Alabama-Oklahoma transform, in *Recent Advances in North American Paleoseismology and Neotectonics East of the Rockies*, edited by R. T. Cox et al., *Geol. Soc. Am. Spec. Pap.*, *493*, 143–164.

Dixon, J. E., T. H. Dixon, D. R. Bell, and R. Malservisi (2004), Lateral variation in upper mantle viscosity: Role of water, *Earth Planet. Sci. Lett.*, *222*, 451–467, doi:10.1016/j.epsi.2004.03.022.

Duncan, R. A. (1984), Age progressive volcanism in the New England seamounts and the opening of the central Atlantic Ocean, *J. Geophys. Res.*, *89*(B12), 9980–9990, doi:10.1029/JB089iB12p09980.

Eaton, D. W., and A. Frederiksen (2007), Seismic evidence for convection-driven motion of the North American plate, *Nature*, *446*(7134), 428–431.

Eaton, D. W., F. Darbyshire, R. L. Evans, H. Grütter, A. G. Jones, and X. Yuan (2009), The elusive lithosphere–asthenosphere boundary (LAB) beneath cratons, *Lithos*, *109*(1), 1–22.

Ebinger, C. J., and N. H. Sleep (1998), Cenozoic magmatism throughout east Africa resulting from impact of a single plume, *Nature*, *395*, 788–791.

Ervin, C. P., and L. D. McGinnis (1975), Reelfoot rift: Reactivated precursor to the Mississippi Embayment, *Geol. Soc. Am. Bull.*, *86*(9), 1287–1295.

Forte, A. M., J. X. Mitrovica, R. Moucha, N. A. Simmons, and P. S. Grand (2007), Descent of the ancient Farallon slab drives localized mantle flow below the New Madrid Seismic Zone, *Geophys. Res. Lett.*, *34*, L04308, doi:10.1029/2006GL027895.

Goes, S., and S. van der Lee (2002), Thermal structure of the North American uppermost mantle inferred from seismic tomography, *J. Geophys. Res.*, *107*(B3), 2050, doi:10.1029/2000JB000049.

Grana, J. P., and R. M. Richardson (1996), Tectonic stress within the New Madrid Seismic Zone, *J. Geophys. Res.*, *101*, 5445–5458, doi:10.1029/95JB03255.

Grand, S. P. (2002), Mantle shear-wave tomography and the fate of subducted slabs, *Philos. Trans. R. Soc. London, Ser. A*, *360*, 2475–2491.

Griffin, W. L., G. C. Begg, D. Dunn, S. Y. O'Reilly, L. M. Natapov, and K. Karlstrom (2011), Archean lithospheric mantle beneath Arkansas: Continental growth by microcontinent accretion, *Geol. Soc. Am. Bull.*, *123*(9/10), 1763–1775, doi:10.1130/B30253.1.

Grollimund, B., and M. D. Zoback (2001), Did deglaciation trigger intraplate seismicity in the New Madrid Seismic Zone?, *Geology*, *29*, 175–178.

Hammond, W. C., and E. D. Humphreys (2000), Upper mantle seismic wave velocity—Effects of realistic partial melt geometries, *J. Geophys. Res.*, *105*(B5), 10,975–10,986, doi:10.1029/2000JB900041.

Hao, Y., K. McIntosh, and M. B. Magnani (2015), Long-lived deformation in the southern Mississippi Embayment revealed by high-resolution seismic reflection and sub-bottom profiler data, *Tectonics*, *34*(3), 555–570, doi:10.1002/2014TC003750.

Hildenbrand, T. G. (1985), Rift structure of the northern Mississippi Embayment from the analysis of gravity and magnetic data, *J. Geophys. Res.*, *90*(B14), 12,607–12,622, doi:10.1029/JB090iB14p12607.

Hildenbrand, T. G., and J. D. Hendricks (1995), Geophysical setting of the Reelfoot Rift and relations between rift structures and the New Madrid Seismic Zone, *U.S. Geol. Surv. Prof. Pap., 1538-E*, 30 pp.

Hildenbrand, T. G., M. F. Kane, and W. Stauder (1977), Magnetic and gravity anomalies in the northern Mississippi Embayment and their spatial relation to seismicity, *U.S. Geol. Surv. Misc. Field Studies Map MF 914*, scale 1:1,000,000.

Hildenbrand, T. G., M. F. Kane, and J. D. Hendricks (1982), Magnetic basement in the upper Mississippi embayment region-a preliminary report, in *Investigations of the New Madrid, Missouri, Earthquake Region*, edited by F. A. McKeown and L. C. Pakiser, *U.S. Geol. Surv., Prof. Pap., 1236*, 39–54.

Hough, S. E., J. G. Armbruster, L. Seeber, and J. F. Hough (2000), On the modified Mercalli intensities and magnitudes of the 1811–1812 New Madrid earthquakes, *J. Geophys. Res.*, *105*, 23,839–23,864, doi:10.1029/2000JB900110.

Huang, J., and D. Zhao (2009), Seismic imaging of the crust and upper mantle under Beijing and surrounding regions, *Phys. Earth Planet. Inter.*, *173*(3), 330–348.

Jacobsen, S. D., J. R. Smyth, H. Spetzler, C. M. Holl, and D. J. Frost (2004), Sound velocities and elastic constants of iron-bearing hydrous ringwoodite, *Phys. Earth Planet. Inter.*, *143*, 47–56.

Johnson, P. R., I. Zietz, and W. A. Thomas (1994), Possible Neo-Proterozoic-Early Paleozoic grabens in Mississippi, Alabama and Tennessee, *Geology*, *22*, 11–14.

Johnston, A. C. (1996), Seismic moment assessment of stable continental earthquakes III. 1811-1812 New Madrid, 1886 Charleston and 1755 Lisbon, *Geophys. J. Int.*, *126*, 314–344.

Kane, M. F. (1977), Correlation of major earthquake centers with mafic/ultra-mafic basement masses, *U.S. Geol. Surv. Prof. Pap., 1028-0*, 199–204.

Kane, M. F., T. G. Hildenbrand, and J. D. Hendricks (1981), Model for the tectonic evolution of the Mississippi Embayment and its contemporary seismicity, *Geology*, *9*(12), 563–568.

Karato, S. I. (1993), Importance of anelasticity in the interpretation of seismic tomography, *Geophys. Res. Lett.*, *20*(15), 1623–1626, doi:10.1029/93GL01767.

Karato, S. I. (2003), Mapping water content in the upper mantle, in *Inside the Subduction Factory*, pp. 135–152, AGU, Washington, D. C., doi:10.1029/138GM08.

Kenner, S. J., and P. Segall (2000), A mechanical model for intraplate earthquakes: Application to the New Madrid Seismic Zone, *Science*, *289*(5488), 2329–2332.

Kennett, B. L. N., and E. R. Engdahl (1991), Traveltimes for global earthquake location and phase identification, *Geophys. J. Int.*, *105*(2), 429–465.

Kuritani, T., E. Ohtani, and J. Kimura (2011), Intensive hydration of the mantle transition zone beneath China caused by ancient slab stagnation, *Nat. Geosci.*, *4*, 713–716.

Lee, C. T. A. (2003), Compositional variation of density and seismic velocities in natural peridotites at STP conditions: Implications for seismic imaging of compositional heterogeneities in the upper mantle, *J. Geophys. Res.*, *108*(B9), 2441, doi:10.1029/2003JB002413.

Li, Z. X., and X. H. Li (2007), Formation of the 1300-km-wide intracontinental orogen and postorogenic magmatic province in Mesozoic south China: A flat-slab subduction model, *Geology*, 179–182.

Lou, X., S. Van der Lee, and S. Lloyd (2013), AIMBAT: A python/matplotlib tool for measuring teleseismic arrival times, *Seismol. Res. Lett.*, *84*, 85–93, doi:10.1785/0220120033.

Mainprice, D., Y. Le Page, J. Rogers, and P. Jouanna (2008), *Ab initio* elastic properties of talc from 1 to 12 GPa: Interpretation of seismic velocities at mantle pressures and prediction of auxetic behavior at low pressure, *Earth Planet. Sci. Lett.*, *274*, 327–338, doi:10.1016/j.epsl.2008.07.047.

Mao, Z., S. D. Jacobsen, D. J. Frost, C. A. McCammon, E. H. Hauri, and T. S. Duffy (2011), Effect of hydration on the single-crystal elasticity of Fe-bearing wadsleyite to 12 GPa, *Am. Mineral.*, *96*, 1606–1612, doi:10.2138/am.2011.3807.

McCamy, K., and R. P. Meyer (1966), Crustal results of fixed multiple shots in the Mississippi Embayment, in *The Earth Beneath the Continents*, *Geophys. Monogr. Ser.*, vol. 10, pp. 370–381, AGU, Washington, D. C.

McKeown, F. A. (1978), Hypothesis—Many earthquakes in the central and southeastern United States are causally related to mafic intrusive bodies, *J. Res. U.S. Geol. Surv.*, *6*(1), 41–50.

Miller, D. J., and N. I. Christensen (1997), Seismic velocities of lower crustal and upper mantle rocks from the slow-spreading Mid-Atlantic Ridge, south of the Kane Fracture Zone (MARK) Proc. Ocean Drill. Program Sci. Results, XX, 437-454.

Mooney, W. D., M. C. Andrews, A. Ginsburg, D. A. Peters, and R. M. Hamilton (1983), Crustal structure of the northern Mississippi embayment and a comparison with other continental rift zones, *Tectonophysics*, *94*, 327–348.

Morris, E. M. (1987), The Cretaceous Arkansas alkali province; a summary of petrology and geochemistry, in *Mantle Metasomatism and Alkaline Magmatism*, edited by E. M. Morris and J. D. Pasteris, *Geol. Soc. Am. Spec. Pap.*, *215*, 217–233, doi:10.1130/SPE215-p217.

Nelson, K. D., and J. Zhang (1991), A COCORP deep reflection profile across the buried Reelfoot Rift, South-Central United States, *Tectonophysics*, *197*, 271–293.

Nuttli, O. W. (1973), The Mississippi valley earthquakes of 1811 and 1812: Intensities, ground motion and magnitudes, *Bull. Seismol. Soc. Am.*, *63*, 227–248.

O'Reilly, S. Y., and W. L. Griffin (2010), The continental lithosphere-asthenosphere boundary: Can we sample it?, *Lithos*, *120*, 1–13, doi:10.1016/j.lithos.2010.03.016.

Paige, C. C., and M. A. Saunders (1982), LSQR: An algorithm for sparse linear equations and sparse least squares, *ACM Trans. Math. Software (TOMS)*, *8*(1), 43–71.

Pollitz, F. F., and W. D. Mooney (2014), Seismic structure of the Central US crust and shallow upper mantle: Uniqueness of the Reelfoot Rift, *Earth Planet. Sci. Lett.*, *402*, 157–166.

Pollitz, F. F., L. Kellogg, and R. Bürgmann (2001), Sinking mafic body in a reactivated lower crust: A mechanism for stress concentration at the New Madrid Seismic Zone, *Bull. Seismol. Soc. Am.*, *91*(6), 1882–1897.

Powell, C. A., M. M. Withers, H. R. DeShon, and M. M. Dunn (2010), Intrusions and anomalous V_p/V_s ratios associated with the New Madrid Seismic Zone, *J. Geophys. Res.*, *115*, B08311, doi:10.1029/2009JB007107.

Pratt, T. L., R. A. Williams, J. K. Odum, and W. J. Stephenson (2013), Origin of the Blytheville Arch, and long-term displacement on the New Madrid Seismic Zone, Central United States, in *Recent Advances in North American Paleoseismology and Neotectonics East of the Rockies*, edited by R. T. Cox et al., *Geol. Soc. Am. Spec. Pap.*, *493*, 1–15.

Pujol, J., A. Johnston, J. M. Chiu, and Y. Yang (1997), Refinement of thrust faulting models for the central New Madrid Seismic Zone, *Eng. Geol.*, *46*, 281–298.

Santosh, M., D. Zhao, and T. Kusky (2010), Mantle dynamics of the Paleoproterozoic North China Craton: A perspective based on seismic tomography, *J. Geodyn.*, *49*(1), 39–53.

Schmandt, B., and F. C. Lin (2014), P and S wave tomography of the mantle beneath the United States, *Geophys. Res. Lett.*, *41*, 6342–6349, doi:10.1002/2014GL061231.

Schutt, D. L., and C. E. Lesher (2006), Effects of melt depletion on the density and seismic velocity of garnet and spinel lherzolite, *J. Geophys. Res.*, *111*, B05401, doi:10.1029/2003JB002950.

Schutt, D. L., and C. E. Lesher (2010), Compositional trends among Kaapvaal Craton garnet peridotite xenoliths and their effects on seismic velocity and density, *Earth Planet. Sci. Lett.*, *300*(3–4), 367–373, doi:10.1016/j.epsl.2010.10.018.

Sigloch, K. (2011), Mantle provinces under North America from multifrequency P wave tomography, *Geochem. Geophys. Geosyst.*, *12*, Q02W08, doi:10.1029/2010GC003421.

Sigloch, K., and M. G. Mihalynuk (2013), Intra-oceanic subduction shaped the assembly of Cordilleran North America, *Nature*, *498*, 50–56, doi:10.1038/nature12019.

Sigloch, K., N. McQuarrie, and G. Nolet (2008), Two-stage subduction history under North America inferred from multiple-frequency tomography, *Nat. Geosci.*, *1*(7), 458–462.

Sleep, N. H. (1997), Lateral flow and ponding of starting plume material, *J. Geophys. Res.*, *102*(B5), 10,001–10,012, doi:10.1029/97JB00551.

Sleep, N. H. (2002), Local lithospheric relief associated with fracture zones and ponded plume material, *Geochem. Geophys. Geosyst.*, *3*(12), 8506, doi:10.1029/2002GC000376.

Sobolev, S. V., and Y. A. Babeyko (1994), Modeling of mineralogical composition, density and elastic wave velocities in anhydrous magmatic rocks, *Surv. Geophys.*, *15*, 515–544.

Sommer, H., and C. Gauert (2011), Hydrating laterally extensive regions of continental lithosphere by flat subduction: A pilot study from the North American Cordillera, *J. Geodyn.*, *51*(1), 17–24.

Sykes, L. R. (1978), Intraplate seismicity, reactivation of preexisting zones of weakness, alkaline magmatism, and other tectonism postdating continental fragmentation, *Rev. Geophys.*, *16*(4), 621–688, doi:10.1029/RG016i004p00621.

Thomas, W. A. (1985), Northern Alabama sections, in *Valley and Ridge Thrust Belt: Balanced Structural Sections, Pennsylvania to Alabama*, edited by N. B. Woodward, pp. 54–61, Univ. of Tennessee, Knoxville, Tenn.

Thomas, W. A. (1991), The Appalachian-Ouachita rifted margin of southeastern North America, *Geol. Soc. Am. Bull.*, *103*, 415–431.

Thomas, W. A. (2006), Tectonic inheritance at a continental margin, *GSA Today*, *16*(2), 4–11, doi:10.1130/1052-5173(2006)016.

Tian, Y., and D. Zhao (2011), Destruction mechanism of the North China Craton: Insight from P and S wave mantle tomography, *J. Asian Earth Sci.*, *42*, 1132–1145, doi:10.1016/j.jseaes.2011.06.010.

Tuttle, M. P., E. S. Schweig, J. D. Sims, R. H. Lafferty, L. W. Wolf, and M. L. Haynes (2002), The earthquake potential of the New Madrid Seismic Zone, *Bull. Seismol. Soc. Am.*, *92*(6), 2080–2089.

Van Arsdale, R., and W. Cupples (2013), Late Pliocene and Quaternary deformation of the Reelfoot Rift, *Geosphere*, *9*(6), 1819–1831.

Van Arsdale, R., R. Bresnahan, N. McCallister, and B. Waldron (2007), Upland complex of the central Mississippi River valley: Its origin, denudation, and possible role in reactivation of the New Madrid Seismic Zone, in *Continental Intraplate Earthquakes: Science, Hazard, and Policy Issues*, edited by S. Stein and S. Mazzotti, *Geol. Soc. Am. Spec. Pap.*, *425*, 177–192.

Van Arsdale, R. B., and R. T. Cox (2007), The Mississippi's curious origins, *Sci. Am.*, *296*(1), 76–82.

Van Arsdale, R. B., H. R. DeShon, and M. P. Tuttle (2012), New Madrid Seismic Zone field trip guide, *Field Guides*, *29*, 123–136.

Van der Lee, S., and A. Frederiksen (2005), Surface wave tomography applied to the North American upper mantle, in *SeismicEarth: Array Analysis of Broadband Seismograms*, *Geophys. Monogr. Ser.*, vol. 157, edited by A. Levander and G. Nolet, pp. 67–80 , AGU, Washington, D. C.

Van der Lee, S., K. Regenauer-Lieb, and D. A. Yuen (2008), The role of water in connecting past and future episodes of subduction, *Earth Planet. Sci. Lett.*, *273*(1), 15–27.

VanDecar, J. C., and R. S. Crosson (1990), Determination of teleseismic relative phase arrival times using multi-channel cross-correlation and least squares, *Bull. Seismol. Soc. Am.*, *80*(1), 150–169.

Villemaire, M., F. A. Darbyshire, and I. D. Bastow (2012), P-wave tomography of eastern North America: Evidence for mantle evolution from Archean to Phanerozoic, and modification during subsequent hot spot tectonism, *J. Geophys. Res.*, *117*, B12302, doi:10.1029/2012JB009639.

Wagner, L. S., M. L. Anderson, J. M. Jackson, S. L. Beck, and G. Zandt (2008), Seismic evidence for orthopyroxene enrichment in the continental lithosphere, *Geology*, *36*(12), 935–938.

Whitmeyer, S. J., and K. E. Karlstrom (2007), Tectonic model for the Proterozoic growth of North America, *Geosphere*, *3*(4), 220–259, doi:10.1130/GES00055.1.

Wolaver, B. D., L. J. Crossey, K. E. Karlstrom, J. L. Banner, M. B. Cardenas, C. G. Ojeda, and J. M. Sharp (2012), Identifying origins of and pathways for spring waters in a semiarid basin using He, Sr, and C isotopes: Cuatrociénegas Basin, Mexico, *Geosphere*GES00849-1.

Xu, Y. G. (2001), Thermo-tectonic destruction of the Archaean lithospheric keel beneath the Sino-Korean Craton in China: Evidence, timing and mechanism, *Phys. Chem. Earth, Part A*, *26*(9-10), 747–757.

Xu, Z., Z. F. Zhao, and Y. F. Zheng (2012), Slab-mantle interaction for thinning of cratonic lithosphere in North China: Geochemical evidence from Cenozoic continental basalts in central Shandong, *Lithos*, *146-147*, 202–217, doi:10.1016/j.lithos.2012.05.019.

Zartman, R. E. (1977), Geochronology of some alkalic rock provinces in eastern and Central United States, *Annu. Rev. Earth Planet. Sci.*, *5*, 257–286.

Zartman, R. E., and J. M. Howard (1987), Uranium-lead age of large zircon rystale from the Potash Sulfur Springs igneous complex, Garland County, Arkansas, in *Mantle Metasomatism and Alkaline Magmatism*, edited by E. M. Morris and J. D. Pasteris, *Geol. Soc. Am. Spec. Pap.*, *215*, 235–240.

Zhang, Q., E. Sandvol, and M. Liu (2009a), Lithospheric velocity structure of the New Madrid Seismic Zone: A joint teleseismic and local P tomographic study, *Geophys. Res. Lett.*, *36*, L11305, doi:10.1029/2009GL037687.

Zhang, Q., E. Sandvol, and M. Liu (2009b), Tomographic Pn velocity and anisotropy structure in the central and eastern United States, *Bull. Seismol. Soc. Am.*, *99*, 422–427.

Zhao, D. (2004), Global tomographic images of mantle plumes and subducting slabs: Insight into deep Earth dynamics, *Phys. Earth Planet. Inter.*, *146*(1), 3–34.

Zhao, D. (2015), *Multiscale Seismic Tomography*, Springer, Jpn.

Zhao, D., A. Hasegawa, and S. Horiuch (1992), Tomographic imaging of P and S wave velocity structure beneath northeastern Japan, *J. Geophys. Res.*, *97*, 19,909–19,928, doi:10.1029/92JB00603.

Zhao, D., A. Hasegawa, and H. Kanamori (1994), Deep structure of Japan subduction zones as derived from local, regional, and teleseismic events, *J. Geophys. Res.*, *99*, 22,313–22,329, doi:10.1029/94JB01149.

Zhao, D., H. Kanamori, and E. Humphreys (1996), Simultaneous inversion of local and teleseismic data for the crust and mantle structure of Southern California, *Phys. Earth Planet. Inter.*, *99*, 191–214.

Zhu, R. X., and T. Y. Zheng (2009), Destruction geodynamics of the North China Craton and its Paleoproterozoic plate tectonics, *Chin. Sci. Bull.*, 3354–3366.

Ziegler, P. A., and S. Cloetingh (2004), Dynamic processes controlling evolution of rifted basins, *Earth Sci. Rev.*, *64*(1), 1–50.